

ARTICLE OPEN



Selective nitrogen doping of graphene due to preferential healing of plasma-generated defects near grain boundaries

G. Robert Bigras¹, X. Glad¹, P. Vinchon¹, R. Martel^{1,2} and L. Stafford¹✉

Hyperspectral Raman IMAGING (RIMA) is used to study spatially inhomogeneous polycrystalline monolayer graphene films grown by chemical vapor deposition. Based on principal component analysis clustering, distinct regions are differentiated and probed after subsequent exposures to the late afterglow of a microwave nitrogen plasma at a reduced pressure of 6 Torr (800 Pa). The $90 \times 90 \mu\text{m}^2$ RIMA mapping shows differentiation between graphene domains (GDs), grain boundaries (GBs), as well as contaminants adsorbed over and under the graphene layer. Through an analysis of a few relevant band parameters, the mapping further provides a statistical assessment of damage, strain, and doping levels in plasma-treated graphene. It is found that GBs exhibit lower levels of damage and N-incorporation than GDs. The selectivity at GBs is ascribed to (i) a low migration barrier of C adatoms compared to N-adatoms and vacancies and (ii) an anisotropic transport of C adatoms along GBs, which enhances adatom-vacancy recombination at GBs. This preferential self-healing at GBs of plasma-induced damage ensures selective incorporation of N-dopants at plasma-generated defect sites within GDs. This surprising selectivity vanishes, however, as the graphene approaches an amorphous state.

npj 2D Materials and Applications (2020)4:42; <https://doi.org/10.1038/s41699-020-00176-y>

INTRODUCTION

Numerous industrial applications of graphene rely on the large-area synthesis, which is commonly achieved by chemical vapor deposition (CVD)¹. This method leads to the formation of numerous grain boundaries (GBs) between graphene domains (GDs). The former has been extensively studied since they are extremely different from GDs with respect to their electronic^{2–4}, mechanical⁵, magnetic⁶, and chemical^{7,8} properties. GBs also have shown both etching enhancement^{9,10} or self-healing¹¹, depending on the irradiation conditions. The understanding of extended defect topology¹² at GBs is limited and quickly vanishes when various growth conditions are considered during irradiation of graphene^{13,14}. As pointed out by Malola et al.⁷ “Grain boundaries [...] are like snowflakes—there is no flake like another”; this clearly highlights their inherent complexity due to a sheer number of different possible GB configurations, each exhibiting its own intrinsic properties^{7,15–17}. This thus makes difficult the study of damage formation by ion or plasma irradiation of polycrystalline graphene films in presence of GBs.

Recently, advances in a non-intrusive spectroscopic technique called hyperspectral Raman imaging (RIMATM—Photon ETC.) have been applied to study the inhomogeneity of plasma-induced disorders in the graphene lattice^{18,19}. This method has been able to detect strong areal differences in polycrystalline monolayer graphene samples grown by CVD that were supposedly highly uniform. Being able to study spatial discrepancies is fundamental since it is well-known that the functionalization of graphene differs according to local defects initially present in the pristine lattice, be it GBs, dislocations, or impurities such as PMMA residues.

Inspired by ref. ¹⁸, the present study capitalizes on RIMA capacities to examine the respective Raman signatures of GDs and GBs following the exposure of polycrystalline monolayer graphene to the late afterglow of a microwave nitrogen plasma at reduced pressure. More precisely, a method based on principal component

analysis (PCA) filtering of hyperspectral Raman mappings¹⁹ is developed and used to analyze behaviors observed in different regions of the CVD-grown graphene samples. The method is able to differentiate clusters that present instances of similar Raman signatures. Thus, it can probe the late-afterglow nitrogen plasma treatment effect on these regions^{20,21}. Coupled with X-ray photoelectron spectroscopy, the doping level of the plasma-treated sample is assessed. By monitoring local variations in the initial pristine state and in the resulting plasma-treated state of the same graphene film, the study sheds light on the dynamical behaviors of N and C adatoms during plasma treatment. Using recent literature, this analysis brings a deeper understanding of doping selectivity in nitrogen plasma treatments.

RESULTS

Imaging and clustering

Graphene samples (grown on copper foil by CVD²² and then transferred on SiO₂/Si substrates using a standard PMMA procedure²³) were exposed to the late-afterglow region of a reduced-pressure plasma sustained by microwave electromagnetic fields^{20,21}. A schematic of the plasma reactor is presented in Supplementary Fig. 1. In this study, the sample undergoes subsequent plasma treatment steps between which the sample is probed by X-Ray photoelectron spectroscopy (XPS) (spot size of 400 microns) and over a $90 \times 90 \mu\text{m}^2$ area using a Raman Imager (RIMATM) from Photon ETC¹⁹. The spatial resolution of Raman measurements is 390 nm. The RIMA allows the acquisition of a high number of spectra (here 116,281) from which parameters of the different bands are extracted. The G ($\sim 1580 \text{ cm}^{-1}$) and 2D ($\sim 2700 \text{ cm}^{-1}$) bands are prominent features of the untreated sample, while the D ($\sim 1350 \text{ cm}^{-1}$) and D' ($\sim 1600 \text{ cm}^{-1}$) bands rise with the generation of plasma-induced disorders²⁴. Typical RIMA measurements, as well as examples of data preparation and processing, are presented in Supplementary Fig. 2 and

¹Département de Physique, Université de Montréal, Montréal, Québec, Canada. ²Département de Chimie, Université de Montréal, Montréal, Québec, Canada. ✉email: luc.stafford@umontreal.ca

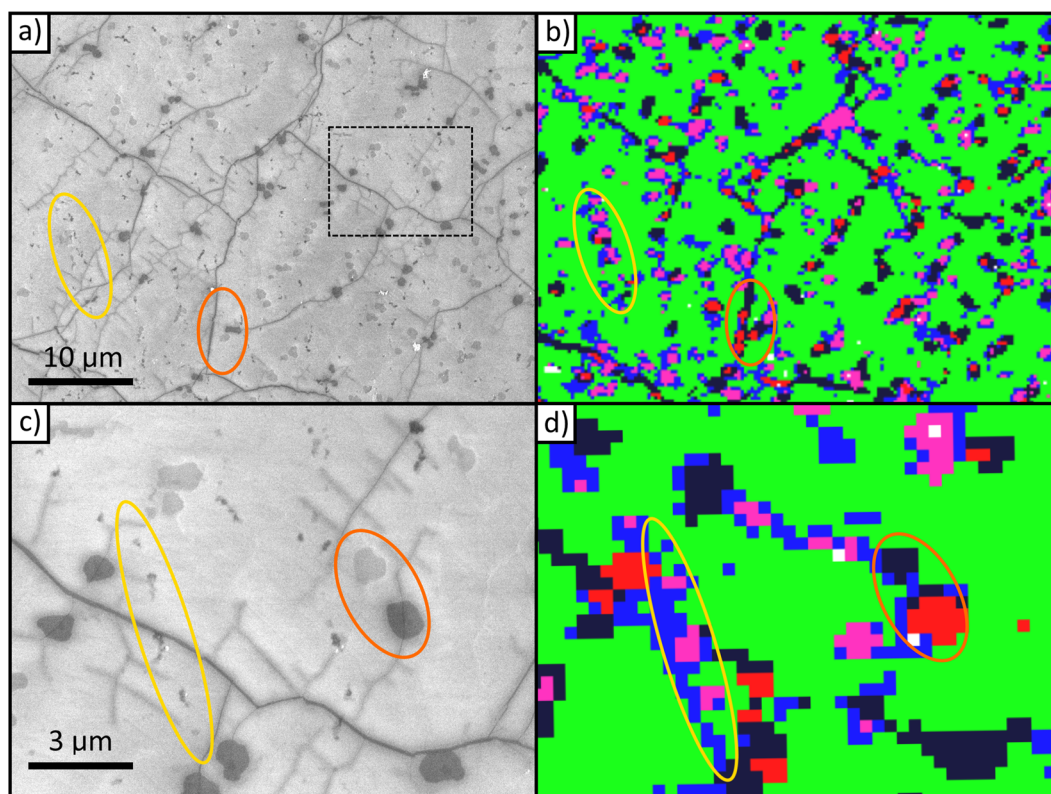


Fig. 1 Graphene surface imaging. **a, c** SEM images of the zone analyzed by hyperspectral Raman (**b, d**) after the last treatment step. Clusters are colored similarly as in the optical images of Supplementary Fig. 1 presented in Supplementary Data. Surface contaminants (yellow circles) are linked to the GSs (blue and purple clusters). GBs and defect spots (orange circle) are a good match with the red and black clusters.

Supplementary Figs. 3 and 4, respectively. PCA-based clustering is performed to highlight the differences between the regions probed inside the RIMA probed area. Scanning electron microscopy (SEM) is carried out after the last plasma treatment to assess the topographical state of the different clusters over the polycrystalline monolayer graphene film.

Figure 1a, c presents SEM images at different magnifications over specific regions of the graphene sample after the final plasma treatment. The clusters identified by PCA analysis over the same regions are shown in Fig. 1b, d. We notice the dominance of the green cluster (72%) matching the graphene domains (GDs). The red (2%) and black (7%) clusters appear to be prevalent at linear defects, seemingly grain boundaries (GBs), and defects in their vicinity. Magenta (5%) and blue (15%) regions are mostly local defective graphene spots (GSs) at the center of the graphene domains. Such comparison thus demonstrates the capability of Raman spectroscopy with RIMA when coupled with a clustering method to highlight the local variation of supposedly uniform monolayer graphene films. Since some of the GSs appear to be indistinguishable from GDs in the SEM images, the clustering technique permits not only to reveal these defective regions but also allows their detailed characterization before and after plasma irradiation. Similar features can be seen by optical imaging over the whole area probed by RIMA analysis. In order to avoid content duplication, the results are presented in Supplementary Fig. 5.

SEM images presented in Fig. 1a–d reveal several topographical features often coinciding with the Raman mapping, in particular the presence of darker lines linked to the boundaries of the various growth domains in polycrystalline graphene films. These lines linked to GBs can also be seen in the comparison between optical image and RIMA cluster mapping presented in Supplementary Fig. 5. Note that, due to the width discrepancy between the Raman pixels (390 nm × 390 nm) and the GBs (typically 2–3 nm

wide²⁵), details seen with SEM (electron beam diameter ~1 nm) may not always be observed in the Raman mapping. Another interesting feature of the SEM images displayed in Fig. 1a, c is the presence of darker circular areas (circled in orange) throughout the whole graphene surface. Typically organized following straight lines, these have a consistent size of ~1 μm in diameter. They also exist in two distinct shades: dark or light gray. As can be seen in Fig. 1c, these regions tend to be crossed by crack-like fractal linear defects emanating from GBs. While they resemble holes in SEM images, their Raman signature (red and black clusters, see all details below) is similar to GBs. These circular features were also examined by Energy-Dispersive X-ray Spectroscopy; the results are shown in Supplementary Note 1. On these darker circular areas, a rise of carbon by about a factor of two with respect to GDs was observed. No significant change in the other elements was seen. This indicates that these dark and light gray spots represent bilayer graphene domains.

Another distinct feature is the presence of numerous isolated dots (highlighted in a yellow circle) spread in a rather uniform way throughout the graphene surface. Considering the surface sensitivity of SEM at 3-kV acceleration voltage (electron penetration depth of about 150 nm in SiO₂²⁶), this could correspond to contaminants introduced either during the growth by CVD and/or through the transfer process of the graphene sample onto SiO₂/Si substrate. Most likely, these dots are mostly contaminants commonly seen in CVD-graphene grown on copper in quartz furnace due to a devitrification of the quartz tube²⁷. When untreated, these carbon-coated SiO_x-based particles appear as small white dots uniformly spread on the untreated surface of the graphene. This aspect was confirmed by Energy-Dispersive X-ray Spectroscopy; the results are also shown in Supplementary Note 1. After plasma treatments and laser exposure (from Raman imaging) of the region of the monolayer graphene film that becomes

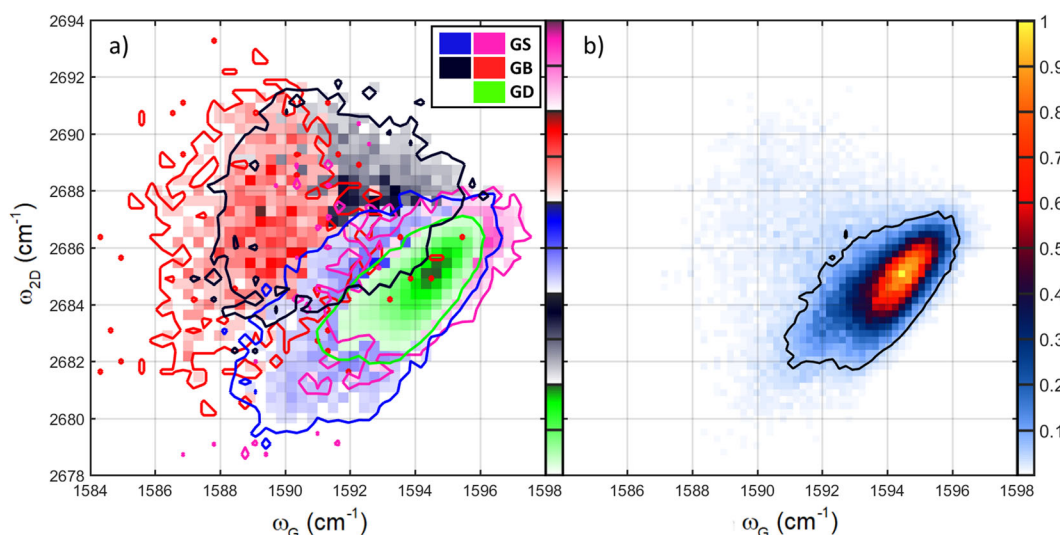


Fig. 2 Doping and strain discrepancies for untreated graphene. **a** Frequency of the 2D band as a function of the frequency of the G band for pristine graphene. Each cluster is depicted as a 2D normalized histogram. **b** Same data as in **a**, but plotted without cluster differentiation.

increasingly amorphous, we noted a change in the morphology of these contaminants (white dots become darker). Graphene surrounding these defects should exhibit modified strain and/or doping, which signals are different in Raman with respect to GDs. Here, these contaminants are linked to the GSs component of the Raman mapping (blue and magenta clusters).

Damage generation

To easily assess relevant properties of CVD-grown graphene films before and after plasma treatment, Raman band parameters can be plotted using normalized 2D histograms such as in Fig. 2a. A maximum count normalization is made, and the observed contours are set at 10% of the maximum for each cluster. This allows to easily highlight how the properties of the graphene differ from a region to another. The red and black clusters present lower G band frequency (ω_G) and higher compressive strain (i.e. higher 2D frequency; ω_{2D}) than the green regions. This is typical of CVD-grown GBs²⁸ and strengthens the aforementioned observation deduced from Fig. 1. The GSs (blue and magenta clusters) and GDs (green) present similar ω_G and ω_{2D} behaviors with a tail at slightly lower values for the former. However, multiple factors can influence band frequency, including doping²⁹ and/or damage³⁰. As discussed below, further investigation is required to identify the nature of these clusters. For comparison purposes, Fig. 2b presents a similar 2D histogram for the full region probed without any cluster differentiation (standard method). In such case, the data do not permit the study of low-count regions. While Raman mappings could help distinguish two regions for a given peak parameter, it cannot do so without parametrization along with two different band parameters. Mean values of Raman band parameters for each cluster are provided in Supplementary Table 11.

A well-established method of characterization of damage generation and damage type in graphene is to plot the ratio of the area of the D and G bands ($A_D:A_G$) as a function of the bandwidth of the G band (Γ_G)³¹. Figure 3 presents such analysis for different successive plasma treatment times of the same graphene sample: $t = 0$ (a), 60 s (b), 120 s = 2×60 s (c), 180 s = 3×60 s (d), and 240 s = 4×60 s (e). The top orange curve is related to pure 0D defect generation (point defects), while the bottom one corresponds to pure 1D defect generation (line defects and reduction of the crystallite sizes)³¹. Due to the change in the coverage ratio of structurally damaged area and activated area, both damage generation pattern (0D or 1D) reveal different Raman signal evolution as the disorder increases. For 0D defects, a sharp rise is

followed by a decrease of $A_D:A_G$ as a function of Γ_G as structurally damaged areas start covering activated areas of nearby defects. This occurs for low inter-defect distances (L_D). The 1D defects show a slower and monotonous increase of $A_D:A_G$ as a function of Γ_G as the size of noncrystalline (L_a) domains decreases.

In Fig. 3a, it can be seen that the GDs (green) of the untreated graphene sample present a very narrow distribution at low Γ_G and $A_D:A_G$, whereas GBs (red and black) show much larger Γ_G while keeping a low $A_D:A_G$. The GS (magenta and blue) data exhibit a rather large $A_D:A_G$ ratio with a rather high and broadly-distributed Γ_G . After the first plasma treatment, Fig. 3b reveals a strong increase of $A_D:A_G$ for the GDs, while Γ_G is rather constant. This corresponds to a strong 0D damage generation to reach about halfway of the 0D-type defect curve. Regarding the GSs, they show a lower $A_D:A_G$ with a slightly higher Γ_G . Most notably, the GBs seem to present a strong sturdiness to the plasma treatment as the $A_D:A_G$ values of the red and black clusters are much lower than the ones of the GDs. This conclusion cannot necessarily be extrapolated to any type of sample as growth conditions can alter the properties of GBs¹². Since each pixel probes, an area far greater than the actual width of GBs ($390 \times 390 \text{ nm}^2$ versus $\sim 2\text{--}3 \text{ nm}^2$), the black and red clusters correspond to areas containing various densities and/or types of GBs⁷.

After two subsequent 60-s treatments (Fig. 3c), the $A_D:A_G$ ratio from GDs reaches the maximum of the empirical 0D defect generation curve ($y \sim 110 \text{ eV}^4$, $x \sim 25 \text{ cm}^{-1}$). At this point, the sample has reached the end of the first stage of damage generation (stage 1^{30–32}). Further damage progressively causes the amorphization of the graphene (stage 2^{30–32}), which is characterized by global disorder with an increasing amount of sp^3 C–C bonds. At the end of stage 1, GBs still show good resistance to the plasma-induced damage, exhibiting both smaller values of Γ_G and $A_D:A_G$ ratios. The last two plasma treatments (Fig. 3d, e) reveal very similar results. As the sample is brought closer to an amorphous state, additional plasma treatments have seemingly less effect on the Raman band parameters^{30,32}. The GDs and GSs show similar signals even though a slight decrease in their $A_D:A_G$ ratios and an increase in their Γ_G (up to 45 cm^{-1}) are observed. On the other hand, GBs show a lower increase in their Γ_G , which is particularly noticeable in the red cluster data.

Figure 3f presents a summary of the clusters' damage generation over all the treatment steps where the mean value for each step and cluster type is plotted (error bars correspond to the standard deviation). The maximum $A_D:A_G$ value for GBs is

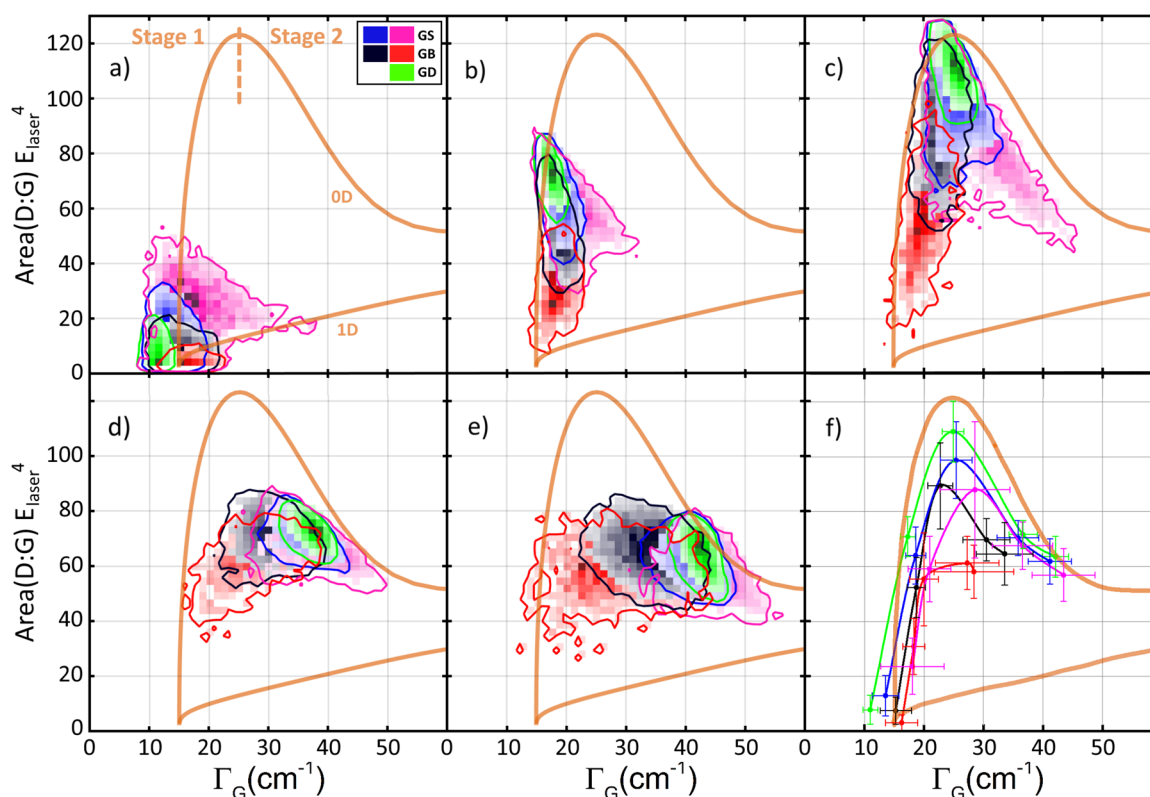


Fig. 3 Damage-type assessment and evolution. Areal ratio of the D over G bands corrected by laser energy as a function of line width of G for $t = 0$ (a), 60 (b), 120 (c), 180 (d), and 240 s (e) of subsequent treatment times on the same zone of the same sample. Top and bottom orange solid lines represent the 0D and 1D type defect generation trajectories, respectively. Average values and error margins for all clusters and all treatment times are shown in (f). Colored lines in (f) are guides to the eye.

much lower than for GDs, whose damaging behavior is close to the empirical 0D damage generation curve (top green curve). This highlights the differences in the damage generation: for GBs, a change in both crystalline sizes (L_a) and inter-defect length (L_D) is present, while GDs essentially see a change in L_D ³¹.

The assessment of the damage with the D:G band ratio for monolayer graphene can be misleading due to its simultaneous dependence on charge carrier density. Indeed, values derived from D:G plots decrease for increasing doping (both positive or negative)^{33,34}. In contrast to the D:G ratio, the D:2D ratio steadily increases with rising lattice disorder³⁵, and its value remains independent upon increasing strain and doping^{34,36}. This explains the recent use of this marker in damage assessment studies in graphene. In this work, the band ratio D:2D is therefore used as a direct indicator of the disordered state of the graphene lattice. Furthermore, the 2D:G ratio is known to be very sensitive to perturbation of the pristine graphene lattice; its value sharply decreases with increasing disorders of any types^{37,38}, including GBs³⁹. The 2D:G ratio also decreases for bi- and multilayer graphene⁴⁰. While 2D:G is also known to be influenced by the doping level³⁴, this ratio (unlike D:G) decreases monotonously with increasing damage and thus facilitates the interpretation of the results. In this framework, Fig. 4 presents the evolution of the 2D:G ratio as a function of the corresponding D:2D ratio.

As can be seen in Fig. 4, almost all clusters present large 2D:G for the untreated sample. This implies the growth of good quality graphene. As expected, a decrease of 2D:G of similar amplitude is found all over the sample after the plasma treatment, but the increase in D:2D is larger for clusters linked to GD and GS regions. This difference of behavior hints towards inhomogeneities in the variation of strain and or doping. Thus GBs seems to undergo a much less aggressive disorder generation: the increase of D:2D

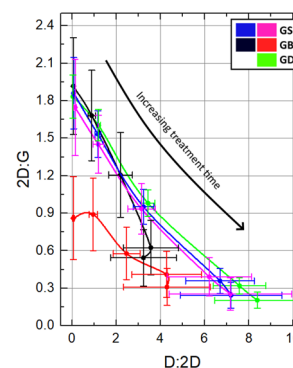


Fig. 4 Graphene disorder. 2D:G as a function of D:2D for each cluster and different total treatment times. Each point is set at the mean value of its respective cluster data with an error bar corresponding to a standard deviation.

from GB-related spectra is two times lower than the one of GDs. Regarding 2D:G, each cluster presents a sharp drop with increasing plasma treatment time with black and red clusters linked to GBs experiencing lower decreases.

Optical strain and doping decoupling

The band frequency variations of G (ω_G) and 2D (ω_{2D}) can provide significant insights into the doping and strain levels of the graphene film. Indeed, the 2D band shows a large shift with a change in lattice strain while its counterpart varies strongly with the graphene doping level^{29,34}. However, the method as proposed by Lee et al. for separating strain and doping²⁹ does not necessarily translate to damaged samples such as those

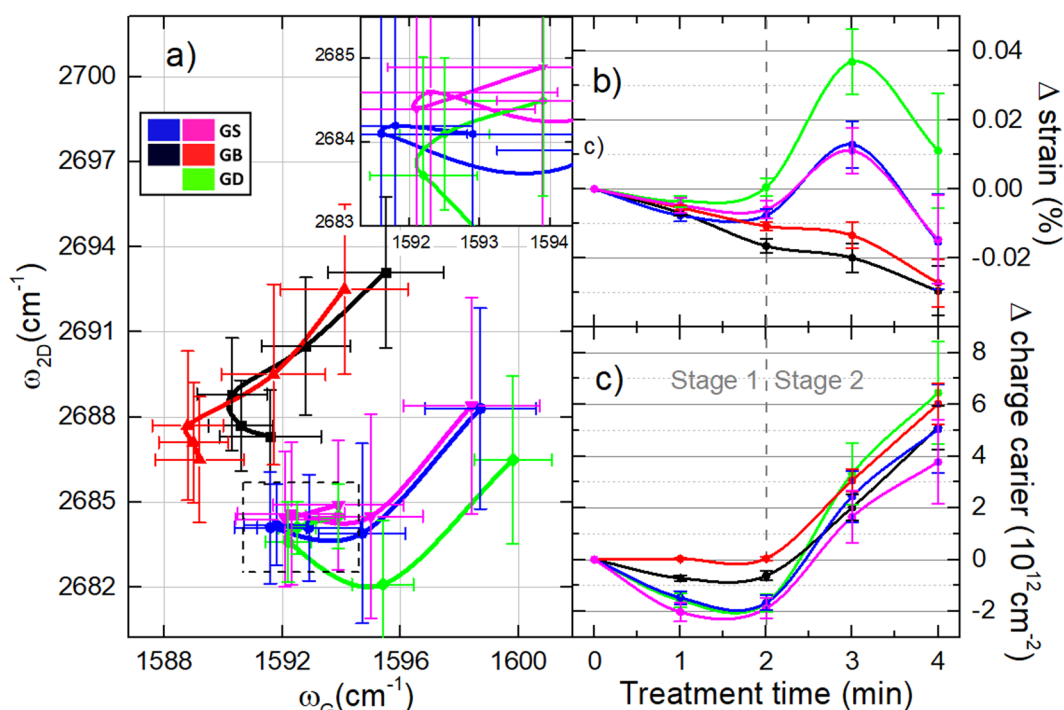


Fig. 5 Optical decoupling of strain and doping. **a** 2D band frequency as a function of G band frequency for all clusters and plasma treatment steps. Each point is set at the mean value of its respective cluster, the standard deviation is taken as the error bar and lines are guides to the eye only. Relative variation in strain (**b**) and charge carrier density (**c**) for each cluster with respect to their pristine state as a function of treatment time. Error bars for (**b**, **c**) show the propagation error of the linear fits (doping and strain) and their projections along the axes defined by Lee et al.²⁹ (corrected for GB clusters).

investigated here since ω_G is also related to defect density for amorphous, nanostructured, and diamond-like carbon sp² materials³⁰. Based on the work of Bruna et al.³⁴, it is possible, however, to extract the behavior of ω_G and ω_{2D} as a function of charge carrier density for damaged graphene (Supplementary Note 2). The linear behavior of ω_{2D} and ω_G highlighted by Lee et al.²⁹ is lost for p-doped damaged graphene. A complete characterization of the band frequency shifts would therefore be required to decouple strain from doping for graphene undergoing increasing disorder. In the current work, the correlation extracted from Bruna et al.³⁴ is used instead since the plasma-induced disorder is relatively important. In such conditions, for n-doped graphene, ω_{2D} becomes proportional to ω_G (Supplementary Note 2). Since we expect the nitrogen plasma to induce n-type doping, this modified method is better adapted, as discussed below. Moreover, Bisset et al.²⁸ revealed the importance of the crystallinity of the sample in the analysis of the ω_G and ω_{2D} variations in response to strain. Indeed, highly polycrystalline CVD-grown samples (crystallite size $L_a \sim 1 \mu\text{m}$) show an increase of ω_G for compressive strain at GBs, as opposed to the decrease observed in exfoliated graphene ($L_a \sim 20 \mu\text{m}$). Since their laser beam diameters are of the order of the CVD-grown graphene domain size, this implies that the x-scale proposed by Lee et al. should be reversed for GB-related data, i.e., for red and black clusters.

In line with these studies, Fig. 5a presents the variation of ω_{2D} and ω_G mean values for all the regions and between the subsequent plasma treatment steps. For ω_G , all regions initially show a small redshift followed by a large blueshift. For ω_{2D} , two distinct behaviors are observed: GBs show a monotonous increase while all other regions undergo a redshift followed by a large blueshift. Figure 5b, c presents the change in doping and strain of each cluster as a function of the plasma treatment time. Such values are obtained by projecting the values of Fig. 5a along the charge carrier density axis introduced by Bruna et al.³⁴, and the strain axis introduced by Bisset et al.²⁸. Only the shifts of the

mean values are considered (to best distinguish the clusters), and the error bars result from the propagation of the errors of the linear fits performed on the relation between strain or charge carrier concentration on Raman band positions (as extracted from the literature^{29,33,34}). In order for any discussion about variations in doping and strain to be relevant, one must first remove the expected effect of damage generation for these conditions. As demonstrated by Eckmann et al.⁴¹, no clear change in ω_G and ω_{2D} should be observed for damaged graphene before the amorphization stage. Entering stage 2 of the amorphization trajectory, the 2D and G bands show large redshifts and blueshifts, respectively. In addition, the effect is much stronger for the 2D band and thus the projection may bias the calculation of the strain from Fig. 5b, but only for the last two treatments and for the heavily damaged clusters (GDs and GSs).

Based on this analysis, the strain and doping behaviors presented in Fig. 5b, c reveal two distinct regimes. The first stage corresponds to a transition from graphene to nanocrystalline graphene (stage 1) and the second to the transition towards amorphous carbon (stage 2)^{30,32,41}. The same transition is highlighted in Fig. 3 (transition towards amorphous carbon is responsible for a decrease of D:G at high disorder levels³¹). More specifically, the first three graphene states along the amorphization trajectory (plasma treatment times: 0, 1, and 2 min) fall into stage 1, in which doping and strain behaviors differ among the different clusters. Most noticeably, the doping of GBs remains constant, while the concentration of charge carriers decreases for the other regions of the sample. This feature provides the first hint of more selective nitrogen incorporation at GDs (so-called segregation of nitrogen dopants at GDs⁴²). In addition, since both p- and n-type dopings increase ω_{2D} and ω_G , a decrease along the axis used for the so-called strain-doping decoupling is related to either a decrease of p- or n-type doping. In Fig. 5c, this doping reduction for GDs and GSs reaches a maximum between 1 and 2 min of plasma treatment. It is usually expected that untreated

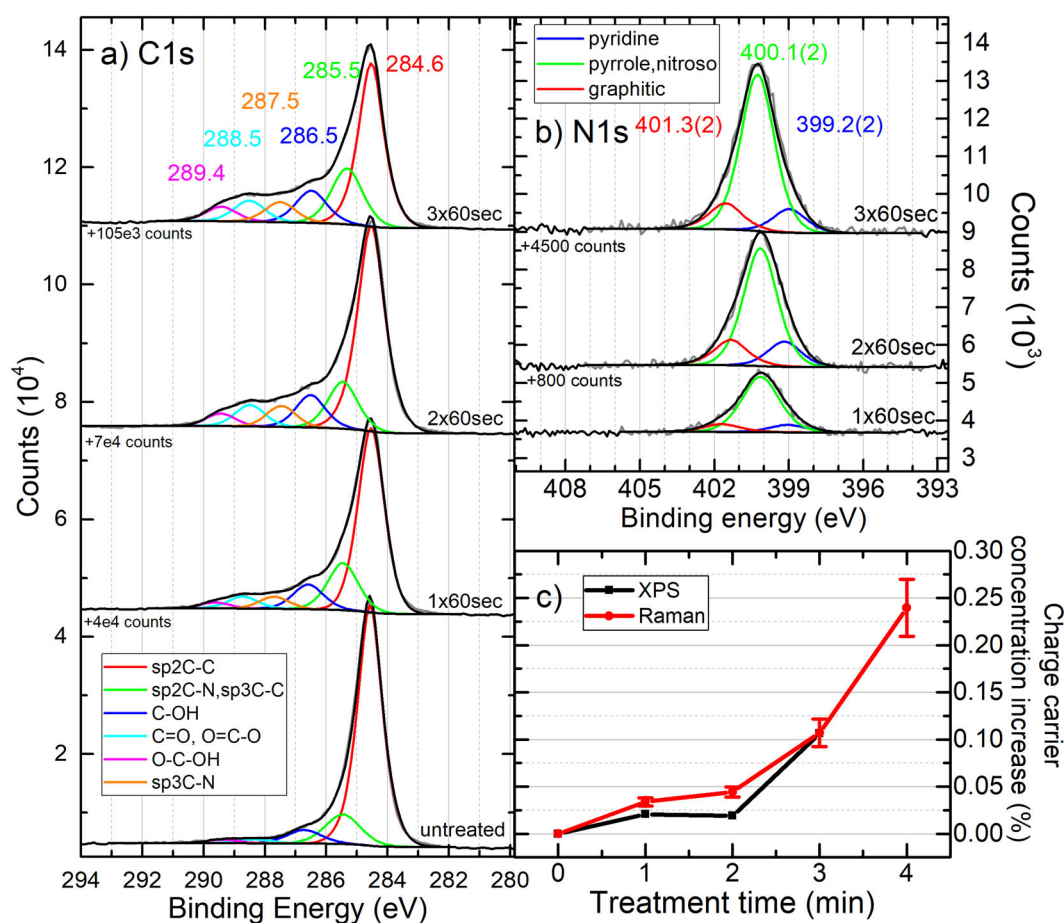


Fig. 6 XPS doping assessment. High-resolution XPS spectra in the regions of C1s (a) and N1s (b) for all sample states. Nitrogen and oxygen bondings to carbon causes the asymmetry of the C1s band. Charge carrier concentration increase (c) as a function of treatment time extracted from Raman data treatments of graphene domains (green cluster) by optical decoupling of strain and doping (red) and XPS graphitic-pyridine inclusion (black).

graphene films grown by CVD show impurity-based (unintentional) p-type doping^{43,44}. Therefore, it can readily be expected that such initial p-type doping first disappears before n-type doping from nitrogen incorporation can appear.

As for the strain evolution during stage 1, it can be seen in Fig. 5b that all clusters sustain a compressive strain with GBs suffering most of that strain. It is worth mentioning that nitrogen incorporation is expected to induce a mild compressive strain to the graphene due to its inferior bond length (C–C: 1.42 Å versus C–N: 1.37 Å⁴⁵). Thus, a doping-related strain is expected to be relatively small for low-to-medium nitrogen incorporation levels⁴⁶. Therefore, the strain features observed in Fig. 5b are most likely due to plasma-induced disorder than to plasma-induced doping in monolayer graphene films.

As discussed above, during the transition toward amorphization (stage 2), ω_{2D} and ω_G are expected to redshift and blueshift, respectively⁴¹. This effect is not considered for the optical separation of strain and doping as it would require criteria to access the transition towards amorphization. As detailed previously and according to Vinchon et al. and Bruna et al.^{11,34}, D:2D is independent of doping, and thus it represents an ideal candidate to discuss qualitatively the effects of an increase of damage on the expected change of the calculated strain (Lee et al.'s model²⁹). According to Eckmann et al.⁴¹, a rise in lattice disorder (in stage 2) leads to a decrease of ω_{2D} and an increase of ω_G with a slope of around $\Delta\omega_{2D}/\Delta\omega_G \sim -1.5$. This would translate in an overall rise of tensile strain (see Fig. 3b of ref. ²⁹), which is consistent with the presence of defects (such as vacancies)

allowing strain relaxation. In our case, Fig. 5b does reveal a rise in tensile strain prior to the amorphization between $t = 1$ and 3 min. In addition, such an increase is not present for the GB-derived clusters (red and black): only a reduction of the decreasing slope is observed. This may be explained by their lower degree of disorder (lower D:2D ratios, Fig. 4), allowing for less strain relaxation than GDs and GSs. Moreover, such an increase of compressive strain might arise due to numerous adatom incorporations leading to inverse Stone-Wales defects⁴⁷. As for the doping in stage 2, it can be seen that the estimated doping level for all clusters follows a similar rise. This rather spatially-uniform change in doping over the entire graphene surface is linked to the transition towards amorphization. More details are provided below.

X-ray photoelectron spectroscopy (XPS) is performed to further support the incorporation dynamics of nitrogen atoms extracted from the decoupling of strain and doping. For each plasma treatment step, XPS is used to extract the N:C ratio and the various components of the N1s high-resolution spectrum. Survey spectra reveal a moderate amount of nitrogen incorporation following subsequent exposure of the graphene films to the late afterglow of microwave N₂ plasmas (N1s/(N1s + C1s) = 3.7%, 5.7%, and 7.6% at 1 min, 2 min, and 3 min of plasma treatment, respectively). XPS surveys are provided in Supplementary Fig. 6. High-resolution spectra of C1s and N1s are presented at Fig. 6a, b. The C1s region presents the main sp² C–C bond typical of graphene at 284.6 eV^{48–53} as well as additional features at higher binding energies related to N bonding (e.g., sp² C=N at 285.5 ± 0.1 eV^{53–55} and sp³ C–N at 287.5 ± 0.1 eV^{55–57}) or O (C–OH at 286.5 ± 0.2 eV^{50–52,57}, C=O and/

or $O=C-O$ at 288.5 ± 0.2 eV^{48,51,55,56,58} and $O=C-OH$ at 289.4 ± 0.2 eV⁵⁷). The N1s region reveals a strong contribution of the pyrrole-imino type of inclusions at 400.1 eV^{53,59–62} with a reasonable amount of pyridine (399.2 eV^{53,54,62,63}) and graphitic incorporations (401.3 eV^{53,54,61–63}). Oxygen inclusion arises due to the exposition to atmospheric conditions of the plasma-related sample between each measurement. Its presence is limited for the untreated sample and is most likely caused by surface contamination²¹. Plasma-induced disorder creates dangling bonds responsible for oxygen inclusion after the treatment and further exposition to ambient air. This contamination is not believed to play a major role in the change in charge carrier concentration or its homogeneities across the graphene surface.

Each nitrogen inclusion is expected to contribute differently to the modification of the Fermi level in monolayer graphene films. While graphitic inclusions induce n-type doping (0.54 e/N), pyridine provides p-type doping (0.45 p/N)⁶⁴. Pyrrole inclusions are less discussed in the literature, but one expects their effects to be limited for low-to-medium nitrogen contents⁶⁵. The product of the nitrogen atomic fraction ($N1s/(N1s + C1s)$) from the survey scans by the respective percent contribution of each nitrogen component from the high-resolution N1s scans is used to estimate the corresponding charge carrier concentration for each plasma treatment step. These results are compared in Fig. 6c to those extracted from Raman optical decoupling of strain and doping, for GDs only. Here, the absolute change in charge carrier density obtained from Raman analysis and presented in Fig. 5c was divided by the atomic density of carbon atoms in graphene domains ($3.85 \times 10^{15} \text{ cm}^{-2}$) to obtain percent variations. (i) Because XPS measurements are spatially averaged, it is impossible to distinguish in XPS the different regions or clusters (as in RIMA), and (ii) GDs represent more than 70% of the graphene surface (see Fig. 1 and Supplementary Fig. 5), it is therefore expected that XPS data are mostly due to GDs. As can be seen in Fig. 6c, similar trends and values are obtained from both XPS and RIMA. However, it is worth highlighting that due to the similar nitrogen content of both graphitic and pyridinic inclusions and their relatively low percent contribution in the overall N1s signals, the corresponding errors in XPS data analysis can be large.

DISCUSSION

Further analysis of the Raman band parameters displayed in the previous section can be used to better understand how each region of the graphene film is altered by the plasma treatment. Despite the use of a reactive plasma source, the analysis proposed by Cancado et al.³¹ still holds and reveals the creation of OD defects at the GDs (Fig. 3). In most plasma irradiation studies, such defects are linked to ion bombardment of the graphene sample. In the late-afterglow region of the microwave nitrogen plasma, however, the kinetic energy of positive ions interacting with the graphene sample (of around 0.5 eV, Supplementary Note 3) is too low to cause any relevant damage. Since pure knock-on collisions can be ruled out in such conditions, other damage formation mechanisms involving local potential energy transfers must be involved⁶⁶, including the surface neutralization of N_2^+ -16 eV, the surface deexcitation of $N_2(A)$ metastable species -6 eV, and the surface recombination of nitrogen atoms -10 eV⁶⁷. Similar energy exchange processes were proposed to reduce the energy barrier by a factor of 4 (from 9 eV to 2.3 eV) for Frenkel pair formation in graphene-like structures under a carbon adatom flux⁶⁸. Note that, over the range of experimental conditions examined in this study, high-energy photons emanating from the main microwave plasma zone cannot reach the late-afterglow region due to the use of an adequately-shaped knee in the discharge tube (Supplementary Fig. 1).

In addition to energy transfer processes, residual oxygen species present in the microwave plasma and flowing afterglow (as a result of base pressure impurities and outgassing of plasma reactor walls)

could also induce mild chemical etching of carbon atoms in monolayer graphene films. Such a phenomenon is expected to be mostly specific to GBs, as previously observed in O- and H-bearing plasmas^{9,69–71}. Surprisingly, GBs reveal less damage generation than all other regions: this is evidenced by a much weaker D:2D ratio at GBs than in GDs. In addition, D:D' ratios are constant for all clusters (Supplementary Fig. 7), suggesting that there is no preferential defect type generation³². Thus, damage formation must either be slower at GBs due to their intrinsic organization or there is a preferential self-healing of plasma-induced damage in these regions. In plasma irradiation conditions leading to a large density of carbon adatoms, Vinchon et al.¹¹ recently revealed that the GBs were more resilient than GDs due to a more efficient Frenkel pair recombination in their vicinity. Briefly, such preferential healing of plasma-generated defects near grain boundaries results from (i) the difference between the migration energy of carbon adatoms (0.4 eV) and vacancies (1.6–3.0 eV)⁷² and (ii) the anisotropic transport of these OD defects along the axis of GBs^{17,73}. This induces an accumulation of carbon adatoms at the GBs, which enhances the probability for adatom-vacancy recombination in the vicinities of GBs. Such a mechanism would obviously result in a net loss of vacancies close to the defect sites of black and red clusters, which explains the low D:2D ratios observed for the latter. This mechanism is expected to vanish as the sample gets more damaged due to the limited transport of C adatoms towards GBs (carbon adatoms now become mostly trapped by disorders in the GDs). Anisotropic transport of carbon adatoms along GBs is also strongly reduced as the graphene approaches the amorphous state. In such conditions, carbon adatoms coverage is expected to become much more uniform. Due to the limited amount of data, however, this transition toward the amorphous state cannot be studied in detail.

As mentioned above, the change in doping extracted from the method presented by Lee et al.²⁹ (updated with measurements of Bissett et al.²⁸ and Bruna et al.³⁴) reveals much larger doping at GDs than at GBs (Fig. 5c). Such dopant segregation at GDs is revealed, while some disorder is induced at GBs. This selective incorporation of nitrogen atoms at GDs only occurs for the first two plasma treatments, i.e. when graphene is still in stage 1 along the amorphization path. The explanation is twofold. First, as evidenced by the observed variations in D:2D ratios (Fig. 4), GDs sustain more damage overall than GBs, the latter being subject to a preferential self-healing phenomenon¹¹. This results in a larger population of vacancies at GDs, which are favored sites for N-atoms incorporation. Second, a crucial aspect of dopant selectivity is the large difference between the migration barrier of carbon and nitrogen adatoms on the graphene surface: 0.4 eV for C⁷² and 1.1 eV for N⁷⁴. This means that C adatoms are highly mobile on monolayer graphene films over the range of experimental conditions investigated here (~room temperature⁷⁵), while N-adatoms are much less mobile. Thus, considering the C adatoms and vacancies behaviors in the study of Vinchon et al.¹¹, a strong population imbalance is expected to arise throughout the sample between C- and N-adatoms with a greater density of carbon adatoms at the GBs. Eventually, as the sample engages its transition towards amorphization (stage 2), the incorporation becomes more homogeneous throughout the whole graphene surface and affects all clusters in a very similar way (Fig. 5c). This inhibits the preferential self-healing mechanism such that the N-incorporation dynamics in stage 2 becomes less selective.

It is worth highlighting that the amplitude of the nitrogen content (3–8%) is similar to what is typically observed for other treatments of CVD-grown monolayer graphene films (1–16%)^{76–78}. The assessment of the electronic doping is not always performed, specially its spatial distribution and its behavior for increasingly disordered graphene. Zhao et al.⁴² have shown the synthesis of N-doped graphene by CVD and have revealed localization of nitrogen incorporation at graphene domains, where a much lower 0.4% graphitic content is shown responsible for n-type doping. Here, plasma-generated nitrogen atoms are found in many more

inclusion configurations, but specific incorporation in the domains is still present even for the much larger nitrogen content.

A combination of Hyperspectral Raman IMager (RIMA) and PCA clustering was used to distinguish different regions of a polycrystalline graphene film grown by CVD and exposed to the late afterglow of a microwave N₂ plasma at low pressure. The precision of the technique, verified by optical microscopy and scanning electron microscopy, is effective in highlighting the evolution of different regions of the sample: graphene domains (GDs), over- and sub-graphene contaminants (GSs) as well as grain boundaries (GBs). Through careful decoupling of strain and doping effects in Raman spectroscopy, selective doping by plasma-generated nitrogen species is revealed at the GDs for the first two plasma treatments. Such dopant segregation is believed to be made possible by a combination of two phenomena. First, a preferential self-healing mechanism occurring at GBs leads to a decrease of the population of vacancies in their vicinity, the latter being a favored site for N-atoms incorporation. Second, an imbalance is expected to occur resulting in a greater density of carbon and nitrogen adatoms at the GBs and GDs, respectively. After the third plasma treatment, the higher defect density throughout the entire graphene surface reduces the mobility of C adatoms toward the GBs, which stop the preferential self-healing mechanism, giving more homogenous N-incorporation across the different regions. Over the range of experimental conditions investigated, n-type doping is evaluated at 0.24%, a result confirmed by X-ray photoelectron spectroscopy. This powerful technique demonstrated the importance of the migration barrier of each plasma-generated defect; accumulating and incorporating more mobile defects in the vicinity of the GBs while defects with higher migration barriers segregate within GDs. These results and the characterization method presented in this study are of particular relevance for the understanding of surface processes in 2D materials and paves the way toward complete tailoring of the doping levels in graphene films.

METHODS

Scanning electron microscopy

Scanning electron microscopy (SEM) were deliberately chosen not to use in between the different steps of plasma irradiation due to the possible electron beam-induced contamination effects⁷⁹. Moreover, the increasingly damaged state of the film after plasma treatment might cause important surface charging effects as the sample gets more amorphous and thus perturbs subsequent Raman analysis. The SEM analysis was performed using a JEOL JSM-7600F in secondary emission mode at 3.0 kV; this allows for a good spatial resolution while ensuring a relatively small electron penetration depth.

X-ray photoelectron spectroscopy

X-ray photoelectron spectroscopy (XPS) is performed to assess the doping level of the polycrystalline monolayer graphene films. The setup is a Thermo Scientific K-Alpha (CAE detector, 180° double-focusing hemispherical analyzer, 128 channel detector) operating with pass energies of 200 eV and 50 eV for a survey and high-resolution scans, respectively. The step energy is 1 eV for the surveys and 0.1 eV for the high-resolution spectra. A flood gun is used to ensure minimal shifts due to charging. The spot size of 400 microns is centered on the area probed by the RIMA system.

Plasma treatment

A gap-type wave launcher (surfatron) maintains a 2.45 GHz surface wave along an 8-mm external (6-mm internal) diameter fused silica discharge tube. The whole apparatus is extensively described in the previous publications^{20,21,80}. In this study, the pressure is set to 6 Torr (800 Pa), the gas flow to 100 standard cube centimeter per minute (scm), and the injected power to 32 W. The resulting plasma length is about 2 cm. From the surfatron gap, the early afterglow peaks at 4 cm while the sample position is set at 27 cm. The sample is far enough from the energetic species of the plasma discharge and thus interacts with a much less

damaging environment. Still, three different reactive species (plasma-generated N atoms, N₂(A) metastable species, and N₂⁺) are present in significant quantities in the afterglow and can induce a significant change of the graphene properties²⁰. Their respective densities in the flowing afterglow region were previously determined by optical emission spectroscopy and Langmuir probe measurements⁸⁰. The setup is presented in Supplementary Information S-I.

RIMA measurements

The setup is detailed elsewhere¹⁸. Briefly, a 3.25-W laser at 532 nm uniformly irradiates a 130 × 130 μm² area via a beam shaping device and a ×100 objective. The resulting Raman emission is then spectrally separated using a volumetric Bragg tunable filter. Despite the beam shaping device, the absolute value mappings of Raman bands still show a large difference between the side and the center of the detector. The line ratio is not affected but the signal to noise varies. In this study, to reduce the effect of a large variation of the signal-to-noise ratio between the center and the sides of the hyperspectral cube, 20-μm bands are cropped from each side resulting in a 90 × 90 μm² final probed area. The RIMA experiments can be time-consuming and thus a 3 × 3 binning is used in order to reduce by a factor 9 the length of each experimental run. Typical unfiltered spectra are presented in Supplementary Information S-II.

Data preparation and processing

The core of the processing methods employed in this article is detailed elsewhere¹⁸. The noise removing algorithm and baseline subtraction was improved. The methods are inspired by the work of Antonelli et al.⁸¹. The following points detail each step.

PCA-based noise filtering

First data centering and normalization are carried out. PCA decomposition (centering) is then applied to extract the first 30 components maps of the measurements. A Gaussian unmixing is used to differentiate the ten clusters core to this study. This is done to ensure that the following noise removal algorithm is able to properly remove the noise of the data of each cluster. Indeed, PCA is intrinsically biased by the intensity of each dimension and therefore mappings containing a low amount of highly distinguishable spectrum induce large error to the noise reduction of these outliers. Moreover, the number of components required to reconstruct all the data would be increased and could possibly reduce the quality of the noise reduction. Base on the work of Antonelli et al.⁸¹, we thus try to remove a uniform simulated noise contribution for the data while ensuring that the noise is similar for all spectra and is of adequate amplitude. We must first estimate the intensity of the noise to be removed. We do so using the modified criteria proposed in another work⁸¹ and do so for each cluster.

$$\text{Experimental noise criterium : } \frac{d^2 \text{err}_{\text{mean}}}{dN^2} < \text{median} \left(\frac{d^2 \text{err}_{\text{mean}}}{dN^2} \right). \quad (1)$$

This criterium is verified for each cluster in order to select the components up to the change in the slope of the average spectrum error. Extreme precision for this first evaluation of experimental noise is not mandatory as a correction of experimental noise is later assessed. We then perform a weighted average of the estimated experimental noise values. To converge toward a more precise value of the experimental noise, we then evaluate a minimum delta value for all clusters simultaneously (adjusting the root mean square of the error by the normalization factor of each cluster). (Eq. (26) from ref. ⁸¹)

$$\text{Delta calculation : } \delta(N_T) = \frac{1}{N} \sum_{j=1}^N \left| \left(e_n(v_j)^2 - e_r(v_j)^2 \right) \right|. \quad (2)$$

This allows to obtain the corrected experimental noise value. Through delta minimization again, we find the number of components in each cluster that allows to remove a constant noise of the appropriate amplitude. Filtered spectra are presented in Supplementary Information S-III.

PCA assisted artifact subtraction

The nature of the artifact of the Raman Imager (RIMA) is yet unknown. Its main cause is believed to be the fluorescence of the system objectives. The shape of the artifact can drastically change from one position to another on the CCD. Measurement is taken on a clean substrate of SiO₂. Through PCA decomposition (centering, no normalization), four main components

are extracted. A linear combination of those can be used to describe the behavior of all the artifacts on the CCD.

Spectrum fitting

It results that four parameters are fitted simultaneously to the band parameters to ensure proper baseline subtraction. The constraints imposed by the 4 core-artifacts enable better fitting of the baseline on the extreme regions of the spectra, i.e., regions where polynomial fitting tends to diverge and somewhat induces error on band fittings. The fitting method is least-square fitting with centering, normalization, and dynamic bounds. Line shapes are set to Lorentzian for all bands. Spectra fitting and artifact subtraction can be assessed for typical spectra presented in Supplementary Information S-III.

PCA clustering

In order to highlight the differences between the regions probed inside the selected area of polycrystalline monolayer graphene films, a processing method was developed. All spectra from the Raman map are first centered using their mean values and normalized according to their standard deviations. PCA is performed using all spectral values as dimensions and after subtraction of the mean values of the spectra. The first 30 components are then separated into 10 clusters using Gaussian unmixing. The number of clusters is arbitrary and is taken high enough to make sure that the most distinguishable regions over the polycrystalline monolayer graphene films are separated into different clusters. The number of components taken for noise filtering is typically lower than 30^{18} and thus the number of considered PCA components is high enough to ensure adequate distinction of the relevant areas. Since the number of components is arbitrary, some clusters are combined by comparing various band parameters (mainly D over G band intensity ratio as well as width and position of the G band). This allows for the definition of final clusters that highlight regions of distinct Raman signatures.

To investigate the evolution of each cluster as the plasma treatment steps are performed, an image registration (allowing only translation and rotation) is carried out to align every plasma-treated measurements relative to the initial region of the untreated graphene sample. This enables a precise study of the evolution of different graphene areas as a function of their initial pristine state (grain boundary, local defects, contaminants, etc.)¹⁸.

DATA AVAILABILITY

The data that support the findings of this study are available from the corresponding author upon request.

Received: 8 June 2020; Accepted: 5 November 2020;

Published online: 04 December 2020

REFERENCES

- Bae, S. et al. Roll-to-roll production of 30-inch graphene films for transparent electrodes. *Nat. Nanotechnol.* **5**, 574–578 (2010).
- Yazyev, O. V. & Louie, S. G. Electronic transport in polycrystalline graphene. *Nat. Mater.* **9**, 806–809 (2010).
- Fei, Z. et al. Electronic and plasmonic phenomena at graphene grain boundaries. *Nat. Nanotechnol.* **8**, 821–825 (2013).
- Yu, Q. et al. Control and characterization of individual grains and grain boundaries in graphene grown by chemical vapour deposition. *Nat. Mater.* **10**, 443–449 (2011).
- Grantab, R., Shenoy, V. B. & Ruoff, R. S. Anomalous strength characteristics of tilt grain boundaries in graphene. *Science* **330**, 946–948 (2010).
- Červenka, J., Katsnelson, M. I. & Flipse, C. F. J. Room-temperature ferromagnetism in graphite driven by two-dimensional networks of point defects. *Nat. Phys.* **5**, 840–844 (2009).
- Malola, S., Häkkinen, H. & Koskinen, P. Structural, chemical, and dynamical trends in graphene grain boundaries. *Phys. Rev. B* **81**, 165447 (2010).
- Yasaie, P. et al. Chemical sensing with switchable transport channels in graphene grain boundaries. *Nat. Commun.* **5**, 4911 (2014).
- Yang, R. et al. An anisotropic etching effect in the graphene basal plane. *Adv. Mater.* **22**, 4014–4019 (2010).
- Nemes-Incze, P., Magda, G., Kamarás, K. & Biró, L. P. Crystallographically selective nanopatterning of graphene on SiO₂. *Nano Res.* **3**, 110–116 (2010).

- Vinchon, P., Glad, X., Robert Bigras, G., Martel, R. & Stafford, L. Preferential self-healing at grain boundaries in plasma-treated graphene. *Nat. Mater.* (2020) <https://doi.org/10.1038/s41563-020-0738-0>.
- Yazyev, O. V. Polycrystalline graphene: atomic structure, energetics and transport properties. *Solid State Commun.* **152**, 1431–1436 (2012).
- Isacson, A. et al. Scaling properties of polycrystalline graphene: a review. *2D Mater.* **4**, 012002 (2016).
- Dong, J. et al. Formation mechanism of overlapping grain boundaries in graphene chemical vapor deposition growth. *Chem. Sci.* **8**, 2209–2214 (2017).
- Biró, L. P. & Lambin, P. Grain boundaries in graphene grown by chemical vapor deposition. *N. J. Phys.* **15**, 035024 (2013).
- Ophus, C., Shekhawat, A., Rasool, H. & Zettl, A. Large-scale experimental and theoretical study of graphene grain boundary structures. *Phys. Rev. B* **92**, 205402 (2015).
- Wang, B., Puzyrev, Y. & Pantelides, S. T. Strain enhanced defect reactivity at grain boundaries in polycrystalline graphene. *Carbon N. Y.* **49**, 3983–3988 (2011).
- Robert Bigras, G. et al. Probing plasma-treated graphene using hyperspectral Raman. *Rev. Sci. Instrum.* **91**, 063903 (2020).
- Gaufrès, E. et al. Hyperspectral Raman imaging using Bragg tunable filters of graphene and other low-dimensional materials. *J. Raman Spectrosc.* **49**, 174–182 (2018).
- Robert Bigras, G., Glad, X., Martel, R., Sarkissian, A. & Stafford, L. Treatment of graphene films in the early and late afterglows of N₂ plasmas: comparison of the defect generation and N-incorporation dynamics. *Plasma Sources Sci. Technol.* **27**, 124004 (2018).
- Robert Bigras, G. et al. Low-damage nitrogen incorporation in graphene films by nitrogen plasma treatment: effect of airborne contaminants. *Carbon N. Y.* **144**, 532–539 (2019).
- Choubak, S., Biron, M., Levesque, P. L., Martel, R. & Desjardins, P. No graphene etching in purified hydrogen. *J. Phys. Lett.* **4**, 1100–1103 (2013).
- Jeong, H. J. et al. Improved transfer of chemical-vapor-deposited graphene through modification of intermolecular interactions and solubility of poly(methylmethacrylate) layers. *Carbon N. Y.* **66**, 612–618 (2014).
- Beams, R., Gustavo Cançado, L. & Novotny, L. Raman characterization of defects and dopants in graphene. *J. Phys. Condens. Matter* **27**, 083002 (2015).
- Ribeiro-Soares, J. et al. Structural analysis of polycrystalline graphene systems by Raman spectroscopy. *Carbon N. Y.* **95**, 646–652 (2015).
- Paqueton, H. & Ruste, J. Microscopie électronique à balayage Principe et équipement. *Tech. l'ingénieur. Anal. caractérisation* (2006).
- Lisi, N. et al. Contamination-free graphene by chemical vapor deposition in quartz furnaces. *Sci. Rep.* **7**, 1–11 (2017).
- Bissett, M. A., Izumida, W., Saito, R. & Ago, H. Effect of domain boundaries on the Raman spectra of mechanically strained graphene. *ACS Nano* **6**, 10229–10238 (2012).
- Lee, J. E., Ahn, G., Shim, J., Lee, Y. S. & Ryu, S. Optical separation of mechanical strain from charge doping in graphene. *Nat. Commun.* **3**, 1024 (2012).
- Ferrari, A. C. & Robertson, J. Interpretation of Raman spectra of disordered and amorphous carbon. *Phys. Rev. B* **61**, 14095–14107 (2000).
- Gustavo Cançado, L. et al. Disentangling contributions of point and line defects in the Raman spectra of graphene-related materials. *2D Mater.* **4**, 025039 (2017).
- Eckmann, A. et al. Probing the nature of defects in graphene by Raman spectroscopy. *Nano Lett.* **12**, 3925–3930 (2012).
- Das, A. et al. Monitoring dopants by Raman scattering in an electrochemically top-gated graphene transistor. *Nat. Nanotechnol.* **3**, 210–215 (2008).
- Bruna, M. et al. Doping dependence of the Raman spectrum of defected graphene. *ACS Nano* **8**, 7432–7441 (2014).
- Jia, K. et al. Effects of defects and thermal treatment on the properties of graphene. *Vacuum* **116**, 90–95 (2015).
- Zhou, Y.-B. B. et al. Ion irradiation induced structural and electrical transition in graphene. *J. Chem. Phys.* **133**, 234703 (2010).
- Martins-Ferreira, E. H. et al. Evolution of the Raman spectra from single-, few-, and many-layer graphene with increasing disorder. *Phys. Rev. B* **82**, 125429 (2010).
- Dresselhaus, M. S., Jorio, A., Souza Filho, A. G. & Saito, R. Defect characterization in graphene and carbon nanotubes using Raman spectroscopy. *Philos. Trans. R. Soc. A Math. Phys. Eng. Sci.* **368**, 5355–5377 (2010).
- Lee, T., Mas'ud, F. A., Kim, M. J. & Rho, H. Spatially resolved Raman spectroscopy of defects, strains, and strain fluctuations in domain structures of monolayer graphene. *Sci. Rep.* **7**, 16681 (2017).
- Das, A., Chakraborty, B. & Sood, A. K. Raman spectroscopy of graphene on different substrates and influence of defects. *Bull. Mater. Sci.* **31**, 579–584 (2008).
- Eckmann, A., Felten, A., Verzhbitskiy, I., Davey, R. & Casiraghi, C. Raman study on defective graphene: effect of the excitation energy, type, and amount of defects. *Phys. Rev. B* **88**, 035426 (2013).
- Zhao, L. et al. Dopant segregation in polycrystalline monolayer graphene. *Nano Lett.* **15**, 1428–1436 (2015).

43. Ahn, Y., Kim, J., Ganorkar, S., Kim, Y.-H. & Kim, S.-I. Thermal annealing of graphene to remove polymer residues. *Mater. Express* **6**, 69–76 (2016).
44. Ryu, S. et al. Atmospheric oxygen binding and hole doping in deformed graphene on a SiO₂ Substrate. *Nano Lett.* **10**, 4944–4951 (2010).
45. Zafar, Z. et al. Evolution of Raman spectra in nitrogen doped graphene. *Carbon N. Y.* **61**, 57–62 (2013).
46. Panchakarla, L. S. et al. Synthesis, structure, and properties of boron- and nitrogen-doped graphene. *Adv. Mater.* **21**, 4726–4730 (2009).
47. Banhart, F., Kotakoski, J. & Krashennnikov, A. V. Structural defects in graphene. *ACS Nano* **5**, 26–41 (2011).
48. Achour, A. et al. Electrochemical anodic oxidation of nitrogen doped carbon nanowall films: X-ray photoelectron and Micro-Raman spectroscopy study. *Appl. Surf. Sci.* **273**, 49–57 (2013).
49. Estrade-Szwarckopf, H. XPS photoemission in carbonaceous materials: a “defect” peak beside the graphitic asymmetric peak. *Carbon N. Y.* **42**, 1713–1721 (2004).
50. Koinuma, M. B. et al. Analysis of reduced graphene oxides by X-ray photoelectron spectroscopy and electrochemical capacitance. *Chem. Lett.* **42**, 924–926 (2013).
51. Siokou, A. et al. Surface refinement and electronic properties of graphene layers grown on copper substrate: An XPS, UPS and EELS study. *Appl. Surf. Sci.* **257**, 9785–9790 (2011).
52. Yang, D. et al. Chemical analysis of graphene oxide films after heat and chemical treatments by X-ray photoelectron and Micro-Raman spectroscopy. *Carbon N. Y.* **47**, 145–152 (2009).
53. Susi, T., Pichler, T. & Ayala, P. X-ray photoelectron spectroscopy of graphitic carbon nanomaterials doped with heteroatoms. *Beilstein J. Nanotechnol.* **6**, 177–192 (2015).
54. Hellgren, N., Haasch, R. T., Schmidt, S., Hultman, L. & Petrov, I. Interpretation of X-ray photoelectron spectra of carbon-nitride thin films: new insights from in situ XPS. *Carbon N. Y.* **108**, 242–252 (2016).
55. Hernández, S. C., Bezares, F. J., Robinson, J. T., Caldwell, J. D. & Walton, S. G. Controlling the local chemical reactivity of graphene through spatial functionalization. *Carbon N. Y.* **60**, 84–93 (2013).
56. Bertóti, I., Mohai, M. & László, K. Surface modification of graphene and graphite by nitrogen plasma: determination of chemical state alterations and assignments by quantitative X-ray photoelectron spectroscopy. *Carbon N. Y.* **84**, 185–196 (2015).
57. Kaciulis, S. Spectroscopy of carbon: from diamond to nitride films. *Surf. Interface Anal.* **44**, 1155–1161 (2012).
58. Datsyuk, V. et al. Chemical oxidation of multiwalled carbon nanotubes. *Carbon N. Y.* **46**, 833–840 (2008).
59. Batich, C. D. & Donald, D. S. X-ray photoelectron spectroscopy of nitroso compounds: relative ionicity of the closed and open forms. *J. Am. Chem. Soc.* **106**, 2758–2761 (1984).
60. Pels, J. R., Kapteijn, F., Moulijn, J. A., Zhu, Q. & Thomas, K. M. Evolution of nitrogen functionalities in carbonaceous materials during pyrolysis. *Carbon N. Y.* **33**, 1641–1653 (1995).
61. Wang, X. et al. N-doping of graphene through electrothermal reactions with ammonia. *Sci. (80-)*. **324**, 768–771 (2009).
62. Scardamaglia, M. et al. Nitrogen implantation of suspended graphene flakes: annealing effects and selectivity of sp² nitrogen species. *Carbon N. Y.* **73**, 371–381 (2014).
63. Ding, W. et al. Space-confinement-induced synthesis of pyridinic- and pyrrolic-nitrogen-doped graphene for the catalysis of oxygen reduction. *Angew. Chem. - Int. Ed.* **52**, 11755–11759 (2013).
64. Schiros, T. et al. Connecting dopant bond type with electronic structure in N-doped graphene. *Nano Lett.* **12**, 4025–4031 (2012).
65. Rybin, M. et al. Efficient nitrogen doping of graphene by plasma treatment. *Carbon N. Y.* **96**, 196–202 (2016).
66. Vinchon, P. et al. A combination of plasma diagnostics and Raman spectroscopy to examine plasma-graphene interactions in low-pressure argon radiofrequency plasmas. *J. Appl. Phys.* **126**, 233302 (2019).
67. Gilmore, F. R. Potential energy curves for N₂, NO, O₂ and corresponding ions. *J. Quant. Spectrosc. Radiat. Transf.* **5**, 369–IN3 (1965).
68. Ewels, C., Heggie, M. & Briddon, P. Adatoms and nanoengineering of carbon. *Chem. Phys. Lett.* **351**, 178–182 (2002).
69. Zhang, Y., Li, Z., Kim, P., Zhang, L. & Zhou, C. Anisotropic hydrogen etching of chemical vapor deposited graphene. *ACS Nano* **6**, 126–132 (2012).
70. Seifert, M. et al. Role of grain boundaries in tailoring electronic properties of polycrystalline graphene by chemical functionalization. *2D Mater.* **2**, 024008 (2015).
71. Xie, L., Jiao, L. & Dai, H. Selective etching of graphene edges by hydrogen plasma. *J. Am. Chem. Soc.* **132**, 14751–14753 (2010).
72. Krashennnikov, A. V. & Nordlund, K. Ion and electron irradiation-induced effects in nanostructured materials. *J. Appl. Phys.* **107**, 071301 (2010).
73. Huang, L. F. et al. Modulation of the thermodynamic, kinetic, and magnetic properties of the hydrogen monomer on graphene by charge doping. *J. Chem. Phys.* **135**, 064705 (2011).
74. Kotakoski, J. et al. B and N ion implantation into carbon nanotubes: insight from atomistic simulations. *Phys. Rev. B* **71**, 205408 (2005).
75. Kang, N., Lee, M., Ricard, A. & Oh, S. Effect of controlled O₂ impurities on N₂ afterglows of RF discharges. *Curr. Appl. Phys.* **12**, 1448–1453 (2012).
76. Wang, H., Maiyalagan, T. & Wang, X. Review on recent progress in nitrogen-doped graphene: synthesis, characterization, and its potential applications. *ACS Catal.* **2**, 781–794 (2012).
77. Fan, M. et al. Recent progress in 2D or 3D N-doped graphene synthesis and the characterizations, properties, and modulations of N species. *J. Mater. Sci.* **51**, 10323–10349 (2016).
78. Inagaki, M., Toyoda, M., Soneda, Y. & Morishita, T. Nitrogen-doped carbon materials. *Carbon N. Y.* **132**, 104–140 (2018).
79. Vadar, A. & Postek, M. Electron beam-induced sample contamination in the SEM. *Microsc. Microanal.* **11**, 764–765 (2005).
80. Afonso Ferreira, J., Stafford, L., Leonelli, R. & Ricard, A. Electrical characterization of the flowing afterglow of N₂ and N₂/O₂ microwave plasmas at reduced pressure. *J. Appl. Phys.* **115**, 163303 (2014).
81. Antonelli, P. et al. A principal component noise filter for high spectral resolution infrared measurements. *J. Geophys. Res. Atmos.* **109**, 1–22 (2004).

ACKNOWLEDGEMENTS

This work was financially supported by the National Science and Engineering Research Council (NSERC), PRIMA-Québec, Plasmionique Inc., Photon ETC., the Fonds de Recherche du Québec - Nature et Technologies (FRQNT), and the Canada Research Chair (L. Stafford and R. Martel). The authors thank Carl Charpin for providing the CVD-grown graphene samples and Charlotte Allard for technical support with Raman imaging.

AUTHOR CONTRIBUTIONS

G.R.B. performed all experimental measurements and the code for the analysis of RIMA data. X.G. and P.V. participated in the initial writing of the paper. All authors contributed to the design of experiments and data interpretation and paper revision. L.S. and R.M. contributed to the funding and supervision of the study.

COMPETING INTERESTS

The authors declare no competing interests.

ADDITIONAL INFORMATION

Supplementary information is available for this paper at <https://doi.org/10.1038/s41699-020-00176-y>.

Correspondence and requests for materials should be addressed to L.S.

Reprints and permission information is available at <http://www.nature.com/reprints>

Publisher's note Springer Nature remains neutral with regard to jurisdictional claims in published maps and institutional affiliations.



Open Access This article is licensed under a Creative Commons Attribution 4.0 International License, which permits use, sharing, adaptation, distribution and reproduction in any medium or format, as long as you give appropriate credit to the original author(s) and the source, provide a link to the Creative Commons license, and indicate if changes were made. The images or other third party material in this article are included in the article's Creative Commons license, unless indicated otherwise in a credit line to the material. If material is not included in the article's Creative Commons license and your intended use is not permitted by statutory regulation or exceeds the permitted use, you will need to obtain permission directly from the copyright holder. To view a copy of this license, visit <http://creativecommons.org/licenses/by/4.0/>.

© The Author(s) 2020